RSC Advances

PAPER

Cite this: *RSC Adv.*, 2016, **6**, 3815

Facile synthesis of Cu_2O microstructures and their morphology dependent electrochemical supercapacitor properties†

Rudra Kumar, Prabhakar Rai* and Ashutosh Sharma*

In this study, Cu_2O microcubes and microspheres were synthesized using facile hydrothermal methods by manipulating the synthesis parameters. The Cu_2O microcubes (~2 μm in diameter) were formed in presence of formic acid, whereas hierarchical Cu_2O microspheres (~5 μm in diameter) were formed in acetic acid. Transmission electron microscopy (TEM) confirmed the formation of single crystalline microcubes and polycrystalline microspheres. The possible growth mechanism suggested that microcubes were formed due to the cubic crystal structure of Cu_2O and the formation kinetics, whereas microspheres were formed due to the orientational attachment of nuclei with similar aggregation velocities along every direction. The electrochemical properties of the Cu_2O microcubes and microspheres were investigated to understand the role of the morphology on the supercapacitor properties. The Cu_2O microcubes exhibited a higher specific capacitance, better rate capability and cycling stability as compared to microspheres, although the particle size and pore size were larger and surface area was lower. The specific capacitance of the Cu_2O microcubes and microspheres were 660 and 516 F g^{-1}, respectively, at a 1 A g^{-1} current density. The Cu_2O microcubes showed 80% specific capacitance retention at a 5 A g^{-1} current density after 1000 cycles. The single crystalline nature and the presence of a smaller number of grain boundaries in the microcubes compared to the microspheres resulted in an increase in conductivity and an increase in capacitance. The results showed that the Cu_2O microcubes can be a promising electrode material for high performance supercapacitors.

Received 1st October 2015
Accepted 15th December 2015

DOI: 10.1039/c5ra20331g

www.rsc.org/advances

Introduction

The overwhelming increase in the human population and urbanization over the past century resulted in the excessive use of natural resources such as fossil fuels to fulfil the energy demand. This has resulted in severe fossil fuel depletion as well as environmental pollution. To overcome these problems, it is desirable to use renewable energy sources, such as solar cells and fuel cells because they are independent of fossil fuels and produce no or little environmental pollution. Therefore, renewable energy sources are expected to play a very important role in this century. To meet the energy demand, rechargeable batteries and supercapacitors as energy storage devices have attracted increasing attention in recent times.[1–4] Among the energy storage devices available, the supercapacitor is one of the most promising candidates because of its high power density and rapid charge discharge rate, as well as excellent cycle stability.[5,6] According to the charge storage mechanism, the supercapacitor is classified into two categories: electric double layer capacitor (EDLCs) and pseudo-capacitors.[7,8] In EDLCs, charge can be stored in the electric double layered formed with the accumulation of electric charge in between the electrode and electrolyte interfaces. Carbon-based materials, such as activated carbon, carbon nanotubes (CNTs) and graphene, store charge in EDLCs with a lower specific capacitance and energy density, which limits the practical applications.[9–14] Pseudo-capacitors store energy by a faradic redox reaction between the electrode material and electrolyte at the electrode surface.[15] Transition metal oxide, metal hydroxides and conducting polymers exhibit pseudo-capacitance behaviour. They possess higher specific capacitance and high energy density compared to EDLCs.[8,16–20]

Among the metal oxides, RuO_2 is used widely as a pseudo-capacitive material owing to its high specific capacitance and high rate capability.[16] However, the toxicity and high cost of RuO_2 prevent its practical use in supercapacitors. Therefore, researchers are devoted to finding other economic and eco-friendly electrode materials for advanced supercapacitors. Recently, less expansive metal oxides, such as MnO_2, V_2O_5, NiO, Fe_3O_4, and Co_3O_4, have been widely used in supercapacitors.[21–25] However, metal oxides have poor electronic conductivity and cycling stability, which limit their use in

---

Department of Chemical Engineering, Indian Institute of Technology Kanpur, Kanpur 208016, India. E-mail: prkrai@iitk.ac.in; ashutos@iitk.ac.in

† Electronic supplementary information (ESI) available: EDS, BET, and EIS characterization of the Cu_2O microcubes and microspheres. See DOI: 10.1039/c5ra20331g

high power supercapacitor devices. The mixing of metal oxide with carbon material with large surface areas and high electrical conductivity is an important approach to overcome this problem. Furthermore, the use of electrode materials in having a battery-type faradaic current profile is another approach to develop high performance supercapacitors.[15] Among the transition metal oxides, copper oxide (CuO and Cu_2O) is another alternative for supercapacitor applications because of its low cost and its potential to provide high specific capacitance.[26–31] Their application in batteries suggests the feasibility of their application in supercapacitors, because similar faradaic redox reactions to those in Li-ion batteries are also used in supercapacitors.[32,33] Among the copper oxides available, cupric oxide (CuO) is used widely for supercapacitor applications.[26–31] These copper oxides have been synthesized by various routes and applied to supercapacitor appliacations.[26–29] Vidyadharan *et al.* reported CuO nanowires synthesised by the electrospinning method as an anode material for supercapacitors.[28] They obtained 620 F g^{-1} specific capacitance in an aqueous electrolyte. Dubal *et al.* synthesised CuO cauliflower by potentiodynamic deposition and copper oxide multilayer nanosheets for supercapacitors with a specific capacitance of 179 F g^{-1} and 43 F g^{-1} in 1 M Na_2SO_4 aqueous electrolyte.[29] However, there are very few reports on cuprous oxide (Cu_2O)-based electrode materials.[34–37] Patake *et al.* reported electrodeposited copper oxide thin film for supercapacitors with maximum specific capacitance of 36 F g^{-1}.[34] Dong *et al.* reports the Cu_2O nanoneedle grown on a Cu foil as a binder free electrode for supercapacitor with an 862 F g^{-1} specific capacitance with excellent cycling stability.[35] Thus, different morphologies of Cu_2O are used to fabricate the electrode, but the effects of the morphology on supercapacitor properties have not been investigated. Although the effect of morphology on supercapacitor property of the anode has been investigated using other materials, a clear relationship between the morphology and property has not been established.[31,38] It is well known that the morphologies of Cu_2O play a vital role in their physical and chemical properties.[39,40] Therefore, in this study, different morphologies of Cu_2O were synthesized *via* a hydrothermal method to examine the effects of morphology on the supercapacitor properties. The morphology of Cu_2O was tuned from cubic to spherical under hydrothermal conditions with the assistance of a capping agent. The cubic shape Cu_2O microstructures showed better capacitance cycling stability than of the spherical microstructure. The crystallinity, particle size, grain boundaries, and electron mobility of the materials have an important role in supercapacitor applications.

Experimental

Material

Copper nitrate trihydrate ($Cu(NO_3)_2 \cdot 3H_2O$), ethanol, formic acid, acetic acid, potassium hydroxide (KOH) were purchased from Fisher Scientific, and nickel foam was purchased from MTI Corporation.

Methods

The synthesis of Cu_2O microstructures was carried out using procedure reported elsewhere with substantial modification.[41] In a typical procedure, $Cu(NO_3)_2 \cdot 3H_2O$ (0.025 M) was dissolved in 30 mL ethanol with vigorous stirring. Equal amounts of (1.5 mL) formic acid or acetic acid were added as a morphology tuner. The solution mixture was sonicated in an ultrasonic water bath for 5 min before the reaction. Finally, the solution was transferred to a Teflon lined stainless steel autoclave, which was filled to 80% of its capacity (40 mL) and the reactions were carried out in an electric oven at 180 °C for 2 h. The brick red (microspheres) or dark purple (microcubes) precipitate was collected and washed several times with distilled water and ethanol and dried at 60 °C for 12 h.

Material characterization

The structural and morphological characterizations of the Cu_2O microcubes and microspheres was measured by field emission scanning electron microscopy (FESEM, ZEISS Supra 40VP, Germany) and transmission electron microscopy (TEM; FEI Tecnai G^2 12 Twin TEM 120 kV). The energy dispersive X-ray spectroscopy (EDX) was performed to determine the elements present in Cu_2O using an Oxford Instruments EDS system attached to the FESEM. The selected area electron diffraction pattern (SAED) was analysed by TEM to determine the amorphous and crystalline nature. The crystal structures of Cu_2O microcubes and microspheres were measured by X-ray diffraction (XRD) (PANalytical, Germany) of Cu Kα radiation (λ = 1.5406 Å) from 5° to 80° at a scanning speed of 2° min^{-1}. Surface area analysis was carried out using the Brunauer–Emmett–Teller (BET) nitrogen adsorption method (Quanta Chrome). Raman spectroscopy (Alpha; Witec, Germany) was analysed in the 50–1000 cm^{-1} frequency range with a 514 nm laser source. The electrical conductivity was measured using a four point conductivity probe (SES Instrument, India), which was attached to a Keithley current source and voltmeter.

Electrochemical measurements

Nickel foam was used as the substrate for the fabrication of the Cu_2O microstructure electrode. The nickel foam was cleaned by degreasing in acetone, etching in 1 M HCl for 15 min, and washing sequentially with water and ethanol for 5 min each. For the fabrication of the working electrode, the Cu_2O microstructures were first mixed with polyvinylidene fluoride (PVDF; Sigma Aldrich) and carbon black (Super P conductive, Alfa Aesar) at a ratio of 75 : 15 : 10. This mixture was stirred in *N*-methyl-2-pyrrolidinone for better homogeneity. The slurry of the Cu_2O microstructures were then pasted on a nickel foam and dried overnight in an oven at 120 °C. The electrochemical measurements were performed in a three-electrode system, in which the Cu_2O microstructure deposited on the nickel foam was used as the working electrode, and Pt rod and Ag/AgCl (3 M KCl) electrodes were used as the counter and reference electrodes, respectively. The geometric surface area of each working electrode was 1 cm^2 and they contained about 1.0 mg of the electroactive material. Cyclic voltammetry (CV), galvanostatic charge–discharge (GCD), and electrochemical impedance spectroscopy (EIS) were carried out in the three-electrode systems. The CV curves were measured from −0.2 to 0.5 V (*vs.* Ag/AgCl) voltage range at the scan rate from 2 to 100 mV s^{-1}. The EIS measurement was tested at the frequency range from 100 kHz to 10 mHz with an AC amplitude of 10 mV under an open circuit potential of 0.01 V. These electrochemical measurements were carried out on a potentiostat/galvanostat (Autolab 302N, Netherlands) at room temperature using a 6 M KOH solution as the aqueous electrolyte. The specific capacitance (C) was calculated from the CV curve using the equation, $C_m = 1/mR\Delta V\int I(v)\,dV$, where C_m is the specific capacitance (F g^{-1}), m is the mass of the active material, R is the scan rate, ΔV is the potential window of scanning and the integral area under the CV curve. In addition, the specific capacitance was calculated by GCD as $C = I\Delta t/m\Delta V$, where C is the specific capacitance in F g^{-1}, I is the current applied in ampere, Δt is the discharge time in second, m is the mass of active material deposited in g and ΔV is the potential window in volts. The energy and power density was calculated from the equation, $E = 1/2CV^2$ and $P = E/t$, respectively, where E is energy density in W h kg^{-1}, P is the power density in W kg^{-1} and t is the discharge time.

Results and discussion

The XRD patterns of the Cu_2O microcubes and microspheres are shown in Fig. 1a. The peaks identified at the 2θ angles of 29.6°, 36.4°, 42.3°, 61.5°, 73.7°, and 77.6° correspond to the (110), (111), (200), (220), (311), and (222) planes of Cu_2O, respectively. All existing peaks confirm the successful formation of the Cu_2O crystal structure and no other phases are detected (JCPDS file no 05-0667). The XRD patterns also show no other impurity-related peaks, which confirm the high purity of both the specimens. The crystallite size of the Cu_2O microstructures was calculated using the Scherrer formula ($t = k\lambda/B\cos\theta$), where t = crystallite size, k = constant dependent on the crystallite shape, λ = X-ray wavelength, B = FWHM, and θ = Bragg angle. The crystallite size of the microcubes and microspheres were 25.2 and 12.3 nm, respectively.

The structural information of the Cu_2O microcubes and microspheres were also studied by Raman scattering and are shown in Fig. 1b. The Raman spectra of both specimens show the characteristic peaks related to the crystalline Cu_2O. The intense peak at 98 cm^{-1} can be assigned to the inactive Raman mode. A shoulder peak at 154 cm^{-1} is recorded in the spectra of both samples, which may be attributed to Raman scattering from the phonons of symmetry Γ_{15}.[42] The strong peak at 218 cm^{-1} and the weak peak at 524 cm^{-1} originated from the Raman-allowed mode of the Cu_2O crystals.[43] The peak at 408 cm^{-1} was assigned to one fourth-order overtone 4 Γ_{12}.[44] The peak related to infrared-allowed mode is recorded at 620 cm^{-1}.[43] Furthermore, the intensity of the band at 218 cm^{-1} is much stronger than those of bands at 154 and 620 cm^{-1}, respectively, indicating that the as-prepared Cu_2O microstructures have a strong enhancement of resonance Raman at 218 cm^{-1}. Thus, the Raman spectra confirm the formation of pure Cu_2O microstructures. In addition, the intensity of Raman peaks of microcube is much higher as compared to microspheres, which indicates the high crystallinity and crystal quality. This result is also supported by the XRD data as the crystallinity of microcubes are higher compared to the microspheres.

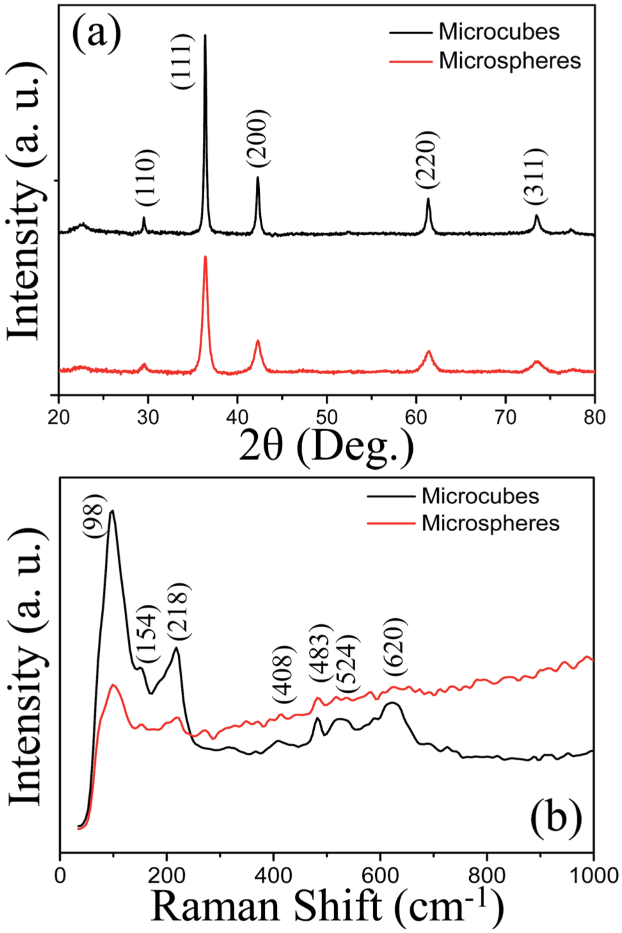

Fig. 1 (a) XRD patterns and (b) Raman spectra of Cu_2O microcubes and microspheres.

The morphology of the as-synthesised Cu_2O microcubes and microspheres were analysed by FESEM and are displayed in Fig. 2. It has been found that cubic shape microstructures are formed in the presence of formic acid under hydrothermal conditions, as shown in Fig. 2a and b. The size of these microcubes was around 2–3 μm. However, some very small cubes can also be found in the FESEM image (Fig. 2a), which suggests that larger cubes are formed due to orientational attachment of smaller cubes. The change in formic acid with acetic acid resulted in the formation of 3–5 μm microspheres, as displayed in Fig. 2c and d. These microspheres appear to be composed of tiny particles, which suggest that these microspheres are formed due to the self-assembly of these tiny particles. These results suggest that formic and acetic acids greatly affected the crystal growth and played a significant role in the formation of these structures. Furthermore, these

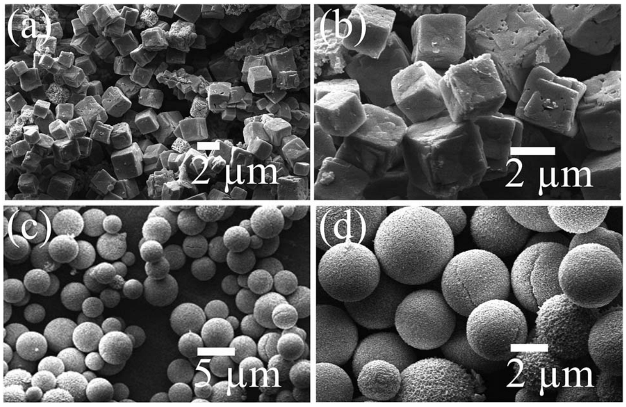

Fig. 2 FESEM images of Cu_2O (a and b) microcubes and (c and d) microspheres.

structures are porous in nature with a rough surface, as visualised in Fig. 2b and d. The composition of the as-synthesized Cu_2O microstructures were analysed by EDS (Fig. S1†), which confirmed the presence of copper and oxygen in the both specimens. The peak for aluminium was present because the materials were deposited on the aluminium foil for FESEM analysis.

Detail structural analysis was carried out by TEM and exhibited in Fig. 3. The TEM images are not clear due to large size of the particles. However, it shows the formation of 2–3 μm microcubes (Fig. 3a), but ~5 μm microspheres (Fig. 3c). Furthermore, the outer surface of the microspheres was rough in nature as compared to the smooth surface of microcubes. The SAED pattern of the microcubes shows some ordered pattern, which confirms the formation of a single crystalline structure (Fig. 3b). However, the presence of a ring pattern in microspheres SAED pattern confirms its polycrystalline nature (Fig. 3d). This suggests that these microspheres are composed of single crystalline nanoparticles. Although the TEM images do not provide a clear image of the microspheres due to its larger particles size, the rough outer surface of microspheres suggests that it may be composed of 10–20 nm primary particles.

The specific surface area of the as-synthesised Cu_2O microcubes and microspheres was analysed by N_2 adsorption desorption measurements and shown in Fig. S2.† The adsorption desorption curve of both specimens can be classified as a type IV isotherm. The BET surface area of the Cu_2O microcubes and microspheres was calculated as 7.39 and 15.28 m^2 g^{-1}, respectively. The presence of a hysteresis loop in the curves of both specimens confirms the presence of mesopores in the samples. The pore size distribution of the Cu_2O microcubes and microspheres was calculated from the Barrett–Joyner–Halenda (BJH) desorption method and shown in the inset in Fig. 2Sa and b,† respectively. Both the specimens were mesoporous in nature as the average pore size distribution was below 50 nm. The average pore size for Cu_2O microcubes and microspheres was 25.7 and 12.8 nm, respectively. The total pore volume of microcubes and microspheres was 0.02 and 0.03 cm^3 g^{-1}, respectively. These results indicate that there is no big difference in surface area, average pore size and pore size volume between the two specimens. However, the pore size and their distributions are favourable for the penetration of electrolytes inside the pores, which can help in the delivery of a high specific capacitance.

The formation of two different morphologies by changing the capping agent suggests that they play an important role as a structure directing agent. A schematic of growth mechanism of Cu_2O microstructure in two different capping agents is shown in Fig. 4. The formic and acetic acids are a weak reducing agent and in the present study, they were used for the reduction of copper nitrate solution to form Cu_2O precipitates.[45,46]

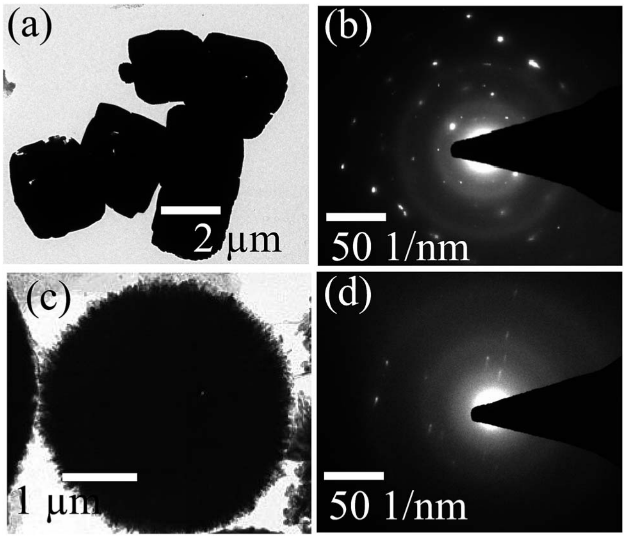

Fig. 3 TEM images along with the SAED pattern of (a and b) microcubes and (c and d) microspheres.

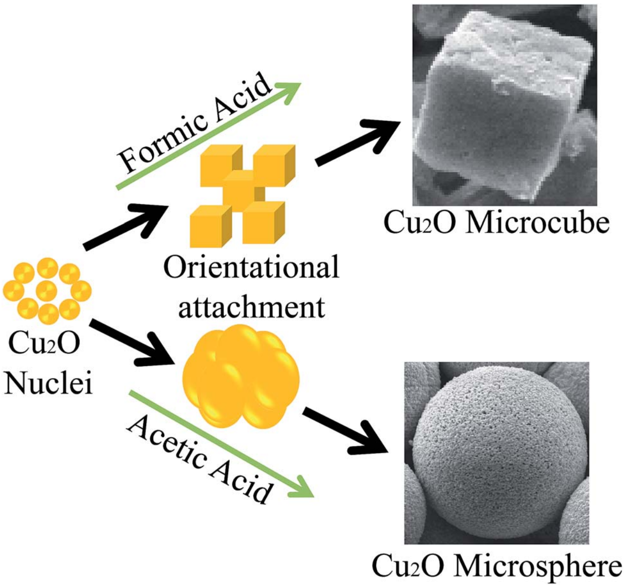

Fig. 4 Schematic of the growth mechanism of Cu_2O microcubes and microspheres.

$$2Cu_{(aq)}{}^{2+} + HCOOH_{(aq)} + H_2O \rightarrow Cu_2O_{(s)} + CO_2 + 4H_{(aq)}{}^{+} \qquad (1)$$

$$2Cu_{(aq)}{}^{2+} + CH_3COOH_{(aq)} + 2H_2O \rightarrow Cu_2O_{(s)} + 2CO_2 + 8H_{(aq)}{}^{+} \qquad (2)$$

In the initial stage, Cu_2O nucleated and grew to nanosized particles. It is well known that the nanoparticles are highly reactive due to the presence of tremendous interfacial energy. Therefore, these nanocrystals aggregated together to form larger particles by the attachment of their high-index planes. This aggregation of nanoparticle to larger ones is thermodynamically feasible, as the reduction in the number of particles decrease the excess energy associated with their interfaces. If the aggregation process can be controlled, then it is possible to produce novel structures. It has been reported that the capping agent can tune the attachment process as well as crystal growth direction due to their selective adsorption to some specific crystal planes of materials. The stability of different crystal faces of Cu_2O in a weak acidic solution falls in the order of (100) ⟫ (111) > (110), which plays a decisive role in the formation of different morphologies of Cu_2O nanocrystals.[47] The morphological evolution always tends to expose the most stable planes as much as possible, which results in the formation of cubic Cu_2O nanocrystals because of the exclusively exposed most stable (100) planes. Therefore, the formation of cubic shape Cu_2O microstructure is related to the cubic crystal structure of Cu_2O and the formation kinetics, and there was little role of formic acid in morphological evolution. Formic acid possibly helped in the orientational attachment of the nanocubes to form microcubes, as evidenced from the SEM image (Fig. 2a). On the other hand, acetic acid plays a different role compared to formic acid because it can complex with terminated "Cu" as a ligand, and therefore prefers to adsorb on certain planes. In the Cu_2O crystal lattice, the (100) plane is highly stable because it is electrically neutral as it is composed of Cu or O atoms only. In contrast, (111) and (110) planes are completely different from the (100) plane of Cu_2O as they are formed with Cu and O atoms and the Cu atoms with dangling bonds, which can make them positively charged. Therefore, acetic acid interacting with the terminated "Cu" of the (110) plane may have changed the growth rate along the [110] direction, and therefore nanoparticles are formed instead of nanocubes. Furthermore, the adsorption of acetic acid on the surface of nanoparticles may have resulted in the formation of microspheres due to same aggregation velocity along every direction. Thus, the chemistry of the capping agent and crystal growth characteristics of Cu_2O are responsible for the formation of these two types of morphologies under hydrothermal conditions.

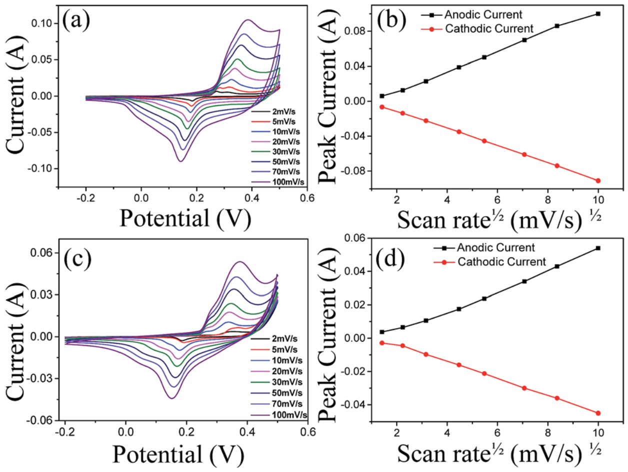

Fig. 5 Electrochemical characterization of the Cu_2O microcubes and microspheres in a 6 M KOH aqueous solution. *CV* curves and corresponding anodic and cathodic peak current *vs.* square root of scan rate of (a and b) microcubes and (c and d) microspheres.

CV analysis of Cu_2O microcubes and microspheres was carried out to investigate their use as an electrode material for supercapacitor applications. The *CV* of Cu_2O microcubes and microspheres at various scan rates are shown in Fig. 5a and c. It shows a linear increase in the electrochemical response current with increasing current rate in both the specimens (Fig. 5b and d). In both devices, the oxidation peak shifted towards a positive potential, while the reduction peak shifted towards a negative potential. This shift in peak position is related to internal resistance of the electrode, which confirms the pseudocapacitive characteristics.[35,48] Indeed, this shift was attributed to an increase in the charge diffusion polarization with the pseudocapacitive electrode.[49] The increase in the current response with the scan rate also suggests that the kinetics of interfacial faradic redox reactions and the rates of electronic and ionic transport are significantly fast even when the scan rate is as high as 100 mV s^{-1}.[50] The specific capacitance from the *CV* curve for Cu_2O microcube and microsphere was 645 F g^{-1} and 545 F g^{-1}, respectively, at a scan rate of 2 mV s^{-1} (Fig. S3†). The detail calculation is reported in ESI.† Furthermore, the specific capacitance decreases gradually with increasing scan rate. The lower capacitance at a high scan rate is due to the limited diffusion and the migration of electrolyte ions at the electrode surface. However, at a lower scan rate, the bulk diffusion of electrolyte ions yields larger capacitance.[28] As shown in the *CV* curve, the anodic peak appears due to the oxidation of Cu_2O microstructure to CuO and $Cu(OH)_2$.[35] The cathodic peak can be ascribed to the reduction of CuO and $Cu(OH)_2$ to Cu_2O. The following reactions between Cu(I) and Cu(II) species exist as described in reactions (3) and (4).

$$Cu_2O + 2OH^- \leftrightarrow 2CuO + H_2O + 2e^- \qquad (3)$$

$$2Cu(OH)_2 + 2e^- \leftrightarrow Cu_2O + 2OH^- + H_2O \qquad (4)$$

Furthermore, in pseudocapacitive materials such as Cu_2O, the relationship of the anodic and cathodic peak current with scan rate determine if the capacitance arises from the surface redox reactions or from the bulk diffusion. Fig. 5b and d show an almost linear relationship, which suggests that the electrode reaction is diffusion-controlled.

The GCD of the Cu_2O microcubes and microspheres at different current densities (1–10 A g^{-1}) are shown in Fig. 6a and b. The specific capacitance was calculated from GCD using the equation, $C_S = It/m\Delta V$, where I, t, m, and ΔV are the applied current, discharge time, active mass of the electrode materials, and voltage window of the charging and discharging, respectively. Fig. 6c shows the specific capacitance as a function of the current density. The specific capacitance of the microcubes was 660, 624, 585, 566, and 550 F g^{-1} at 1, 3, 5, 8, and 10 A g^{-1}, respectively. However, the specific capacitance of the microspheres was 516, 448, 408, 377, and 357 F g^{-1} at 1, 3, 5, 8, and 10 A g^{-1}, respectively. These results confirm that the microcubes contribute higher specific capacitance and better rate capability. In addition, the long-term cycle stability of the microcubes and microspheres was also investigated by repeating the GCD. Fig. 6d shows the cycling performance of the microcubes and microspheres at a current density of 10 A g^{-1} for 1000 cycles. The specific capacitance of microcubes was 295 F g^{-1} (55% capacitance retention), whereas the microspheres was 172 F g^{-1} (42% capacitance retention) after 1000 charge–discharge cycle at a current density of 10 A g^{-1}. The specific capacitance of the microcubes was 550 F g^{-1} (80% capacitance retention) after 1000 cycles, when the current density was decreased from 10 to 5 A g^{-1} (Fig. S4†). The specific capacitance loss occurs due to the mechanical expansion of the electrode material during the charging and discharging process and the small amount of dissolution of some electrode materials during cycling.[51] The lower loss in specific capacitance of the microcubes as compared to microspheres is possibly related to its single crystalline nature. The supercapacitor performance of Cu_2O microcubes was compared with similar system reported elsewhere, which shows that Cu_2O microcubes have the potential to be used as an electrode for supercapacitor applications (Table S1†).

The power density and energy density can be further calculated from the GCD. For the Cu_2O microcubes, the energy densities were 14.6, 13.5, 12.8, and 12.2 W h kg^{-1}, and the power densities were 200, 800, 1400, and 2000 W kg^{-1} at current densities of 1, 4, 7, and 10 A g^{-1}, respectively. For the Cu_2O microspheres, the energy densities were 11.4, 9.5, 8.6, and 7.9 W h kg^{-1}, and the same power densities at current densities of 1, 4, 7, and 10 A g^{-1}, respectively. Thus, the energy and power densities of the microcubes are better than microspheres.

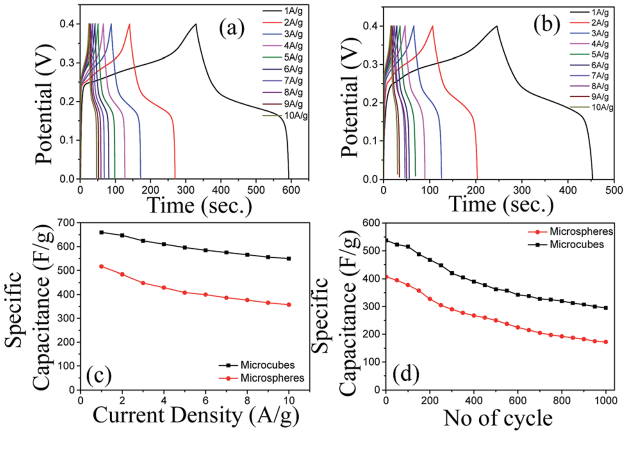

Fig. 6 GCD curves of the Cu_2O (a) microcubes and (b) microspheres, (c) specific capacitance of the microcubes and microspheres as a function of current density and (d) cycling performance and coulombic efficiency of microcubes and microspheres at a constant current density of 10 A g^{-1}.

Furthermore, the effects of the electrolyte concentration on supercapacitor properties have been investigated and results are shown in Fig. S5.† The *CV* curve of Cu_2O microcubes at 1, 3 and 6 M KOH electrolyte concentration at a 50 mV s^{-1} scan rate are shown in Fig. S5a.† The concentration of KOH has a significant effect on the profile of the *CV*s. As shown in figure, the area swept by the *CV* curve increases with increasing KOH concentration.[52] The charges corresponding to anodic and cathodic peak increase with increasing KOH concentration. These effects show that a higher specific capacitance can be achieved with an increase in electrolyte concentration. The cycling stability of the Cu_2O microcubes up to 500 cycles at a 50 mV s^{-1} scan rate is displayed in Fig. S5b.† It shows very small diminishing of anodic and cathodic peaks, which indicates that the Cu_2O microcubes are excellent candidates for supercapacitor electrode materials. The galvanostatic charge–discharge curve at different electrolyte concentrations is shown in Fig. S5c.† The longer discharge time at a higher KOH concentration shows higher specific capacitance, which is consistent with the *CV* curve. The specific capacitance of the 1 and 3 M KOH concentration was 110 and 380 F g^{-1}, respectively, as shown in Fig. S5d.† Furthermore, the coulombic efficiency was calculated using the equation, $\eta = (t_d/t_c) \times 100$, where, t_d = galvanostatic discharge time and t_c = galvanostatic charge time. The coulombic efficiency was nearly constant at 90% within 1000 cycles, as shown in Fig. S6.†

EIS was performed to determine the charge kinetics of the electrode materials by applying an AC voltage with a 10 mV amplitude over a frequency range from 0.01 Hz to 100 kHz (Fig. S7†). The series resistance (R_s) in the EIS plot measured at the high frequency region corresponds to the intrinsic resistance of the electroactive electrode material, bulk resistance of the electrolyte, and the contact resistance between the electrolyte and electrode at the interface. The charge transfer resistance (R_{ct}) can be measured from the diameter of the semicircle from the high frequency range. The slope of the EIS curve in the low frequency range reflects the Warburg resistance (R_w), which describes the diffusion of redox species in the electrolyte solution. The EIS plot of the microcubes and microspheres is shown in Fig. S7a.† The steeper vertical line of the microcubes shows better capacitive behaviour compared to the microspheres. The series resistance of the Cu_2O microcubes and microspheres was 1.26 Ω and 1.4 Ω, respectively, indicating the improved electrical conductivity of the Cu_2O microcubes. A small semi-circle was observed for microcubes and microspheres in the high frequency region (Fig. S7b and c†), which can be used to calculate the charge transfer resistance. The R_{ct} values were 0.8 and 1.2 Ω for the microcubes and microspheres, respectively. These parameters indicate the good electrical conductivity and ion-diffusion behavior of the electrodes. The low R_s and R_{ct} value of microcubes compared to the microspheres reflects the low charge transfer resistance and better mass transfer. In addition, the relatively lower equivalent series resistance (ESR) of the Cu_2O microcubes could be attributed to its morphology and superior crystallinity. This result was supported further by the I–V curve measurement of the Cu_2O microcubes and microspheres (Fig. S8†). The specimen for measurement was prepared by making a pellet. The pellet was made by mixing the Cu_2O microstructures with polyvinylidene fluoride and carbon black in the ratio 75 : 15 : 10. The resistivity was calculated using the equation, $\rho = 4.52 \times (V/I) \times t$, where ρ, V, I, and t are the resistivity (Ω cm), voltage (V), current (A), and thickness (cm) of the electrode, respectively. The electrical conductivity was calculated as $\sigma = 1/\rho$, where σ is the electrical conductivity (S cm^{-1}).[53] The conductivity of the Cu_2O microcubes and microspheres were 0.273×10^{-3} and 0.189×10^{-3} S m^{-1}, respectively. Thus, the Cu_2O microcubes are more conducting as compared to the microspheres.

The enhanced electrochemical performance of the Cu_2O microstructure is related to its structure, which has shorten the diffusion of electrons and ions and resulted in reduced internal resistance and charge transfer resistance. Furthermore, the 3-dimensional (3D) structure of the Ni foam conductive substrate can provide fast electronic transfer channels and exhibit more active reaction sites with the electrolyte to participate in the fast redox reactions and display stronger adhesion with the current collector to improve the electrochemical performance.[28,54] Interestingly, the microcubes show better specific capacitance and cycling property than the microspheres, even though its surface area is lower and pore size is wider. The electrochemical performance depends mainly on the surface area, pore size, crystallinity, and electrical conductivity.[55] The crystallinity of the materials may play an important role, and the microcubes show better electrochemical performance due to their single crystalline nature. The poor cycling property of microspheres is due to its polycrystalline nature, which is highly defective due to the presence of a large number of grain boundaries. The presence of grain boundaries also affects the electrical conductivity, as the electrical conductivity depends on the density and mobility of the charge carriers in a material. The charge carrier mobility depends on all inelastic scattering processes through which current flow is impeded. The presence of grain boundaries in a material results in the scattering of charge carriers at the interfaces between grains (Fig. 7). Therefore, the movement of an electric current is often far from the idealized picture under the influence of an applied electric field, if the grain boundaries are present in the material.[56]

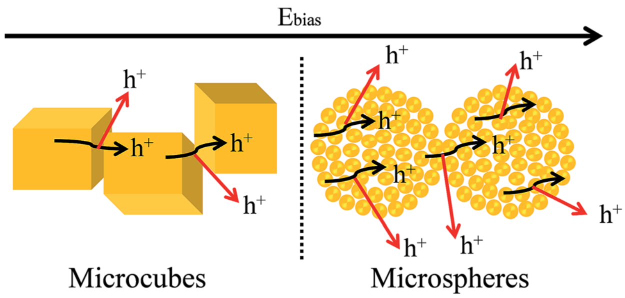

Fig. 7 Conduction of current in the Cu_2O microcubes and microspheres containing grain boundaries.

Tamaki *et al.* proposed a relationship between the number of grains and the resistance, which state that the resistance is directly proportional to the number of grains between the two electrodes.[57]

$$R_a = 2R_a(i) + (N - 1)\, R_a(gb) = (2R_a(i) - R_a(gb)) + R_a(gb)N \qquad (5)$$

herein, $R_a(i)$ and $R_a(gb)$ are the resistance at interface and grain boundary in air, respectively, and N is the number of grains included in the gap. Because the microspheres are polycrystalline in nature and their crystallite size is smaller than the microcubes, the number of grain boundaries could be higher. Thus, the electrical conductivity of the microcubes will be better than in the microspheres. However, this is a preliminary study and more detail study will be needed to fully understand the morphology–supercapacitance relationship. Overall, these results demonstrate the high specific capacitance and excellent cycling property of the Cu_2O microcubes, and thereby making them a promising electrode material for supercapacitor applications.

Conclusions

In summary, we successfully synthesized mesoporous Cu_2O microcubes and microspheres using a one pot hydrothermal method by varying the synthesis parameters. The mesoporous Cu_2O microcubes and microspheres were assembled by the orientational growth of nuclei. Compared to the microsphere, microcubes were smaller in size and single crystalline in nature, but the surface area of the microspheres was higher. The electrochemical properties of these materials were investigated for applications as an electrode in supercapacitors. The Cu_2O microcubes displayed higher specific capacitance, better rate capability and cycling stability than the microspheres. The effect of the morphology on the supercapacitor property suggested that microcubes with a single crystalline nature and lower number of grain boundaries resulted in an increase in electrical conductivity, and therefore improvement in electrochemical performance. These results show that the mesoporous Cu_2O microcubes have great potential for use as an advanced electrode material for high-performance supercapacitors.

Acknowledgements

This study was supported by the Department of Science and Technology (DST), New Delhi, India vide DST-INSPIRE Faculty Scheme (DST/INSPIRE/04/2014/001318). We acknowledge the use of characterization facilities at Thematic Unit of Excellence on Soft Nanofabrication with Application in Energy, Environment and Bioplatform and Advanced Imaging Centre at IIT Kanpur.

Notes and references

1 J. R. Miller and P. Simon, *Science*, 2008, **321**, 651–652.

2 M. Armand and J. M. Tarascon, *Nature*, 2008, **451**, 652–657.

3 P. Simon and Y. Gogotsi, *Nat. Mater.*, 2008, **7**, 845–854.

4 M. Winter and J. R. Brodd, *Chem. Rev.*, 2004, **104**, 4245–4270.

5 G. P. Wang, L. Zhang and J. J. Zhang, *Chem. Soc. Rev.*, 2012, **41**, 797–828.

6 L. L. Zhang and X. S. Zhao, *Chem. Soc. Rev.*, 2009, **38**, 2520–2531.

7 E. Frackowiak and F. Beguin, *Carbon*, 2001, **39**, 937–950.

8 L. Huang, D. Chen, Y. Ding, S. Feng, Z. L. Wang and M. Liu, *Nano Lett.*, 2013, **13**, 3135–3139.

9 H. C. Liang, F. Chen, R. G. Li, L. Wang and Z. H. Deng, *Electrochim. Acta*, 2004, **49**, 3463–3467.

10 Y. Wang, Z. Q. Shi, Y. Huang, Y. F. Ma, C. Y. Wang, M. M. Chen and Y. S. Chen, *J. Phys. Chem. C*, 2009, **113**, 13103–13107.

11 C. Yu, C. Masarapu, J. Rong, B. Wei and H. Jiang, *Adv. Mater.*, 2009, **21**, 4793–4797.

12 J. Liu, L. Zhang, H. B. Wu, J. Lin, Z. Shen and X. W. Lou, *Energy Environ. Sci.*, 2014, **7**, 3709–3719.

13 J. Liu, J. Sun and L. Gao, *J. Phys. Chem. C*, 2010, **114**, 19614–19620.

14 M. F. El-Kady, V. Strong, S. Dubin and R. B. Kaner, *Science*, 2012, **335**, 1326–1330.

15 P. Simon, Y. Gogotsi and B. Dunn, *Science*, 2014, **343**, 1210–1211.

16 Z. S. Wu, D. W. Wang, W. Ren, J. Zhao, G. Zhou, F. Li and H. M. Cheng, *Adv. Funct. Mater.*, 2010, **20**, 3595–3602.

17 Z. B. Lei, J. T. Zhang and X. S. Zhao, *J. Mater. Chem.*, 2012, **22**, 153–160.

18 W. Yang, Z. Gao, J. Ma, X. Zhang and J. Wang, *J. Alloys Compd.*, 2014, **611**, 171–178.

19 Y. Y. Gao, S. L. Chen, D. X. Cao, G. L. Wang and J. L. Yin, *J. Power Sources*, 2010, **195**, 1757–1760.

20 A. Sumboja, X. Wang, J. Yan and P. S. Lee, *Electrochim. Acta*, 2012, **65**, 190–195.

21 V. Subramanian, H. W. Zhu and B. Q. Wei, *J. Power Sources*, 2006, **159**, 361–364.

22 H. Y. Lee and J. B. Goodenough, *J. Solid State Chem.*, 1999, **148**, 81–84.

23 C. Z. Yuan, X. G. Zhang, L. H. Su, B. Gao and L. F. Shen, *J. Mater. Chem.*, 2009, **19**, 5772–5777.

24 J. Chen, K. L. Huang and S. Q. Liu, *Electrochim. Acta*, 2009, **55**, 1–5.

25 L. Cui, J. Li and X. G. Zhang, *J. Appl. Electrochem.*, 2009, **39**, 1871–1876.

26 K. Krishnamoorthy and S.-J. Kim, *Mater. Res. Bull.*, 2013, **48**, 3136–3139.

27 Y. X. Zhang, M. Huang, F. Li and Z. Q. Wen, *Int. J. Electrochem. Sci.*, 2013, **8**, 8645–8661.

28 B. Vidyadharan, I. Misnon, J. Ismail, M. M. Yusoff and R. Jose, *J. Alloys Compd.*, 2015, **633**, 22–30.

29 G. J. Navathe, D. S. Patil, P. R. Jadhav, D. V. Awale, A. M. Teli, S. C. Bhise, S. S. Kolekar, M. M. Karanjkar, J. H. Kim and P. S. Patil, *J. Electroanal. Chem.*, 2015, **738**, 170–175.

30 D. P. Dubal, G. S. Gund, C. D. Lokhande and R. Holze, *Mater. Res. Bull.*, 2013, **48**, 923–928.

31 B. Heng, C. Qing, D. Sun, B. Wang, H. Wang and Y. Tang, *RSC Adv.*, 2013, **3**, 15719–15726.

32 C. Wang, D. Higgins, F. Wang, D. Li, R. Liu, G. Xia, N. Li, Q. Li, H. Xu and G. Wu, *Nano Energy*, 2014, **9**, 334–344.

33 K. Chen, S. Song and D. Xue, *CrystEngComm*, 2015, **17**, 2110–2117.

34 V. D. Patake, S. S. Joshi, C. D. Lokhande and Q.-S. Joo, *Mater. Chem. Phys.*, 2009, **114**, 6–9.

35 C. Dong, Y. Wang, J. Xu, G. Cheng, W. Yang, T. Kou, Z. Zhang and Y. Ding, *J. Mater. Chem. A*, 2014, **2**, 18229–18235.

36 X. Dong, K. Wang, C. Zhao, X. Qian, S. Chen, Z. Li, H. Liu and S. Dou, *J. Alloys Compd.*, 2014, **586**, 745–753.

37 B. Li, H. Cao, G. Yin, Y. Lua and J. Yin, *J. Mater. Chem.*, 2011, **21**, 10645–10648.

38 S. K. Meher, P. Justin and G. R. Rao, *Nanoscale*, 2011, **3**, 683–692.

39 J.-Y. Ho and M. H. Huang, *J. Phys. Chem. C*, 2009, **113**, 14159–14164.

40 X. Wan, J. Wang, L. Zhu and J. Tang, *J. Mater. Chem. A*, 2014, **2**, 13641–13647.

41 Y. Chang and H. C. Zeng, *Cryst. Growth Des.*, 2004, **4**, 273–278.

42 A. Compaan and H. Z. Cummins, *Phys. Rev. Lett.*, 1973, **31**, 41.

43 D. Powell, A. Compaan, J. R. Macdonald and R. A. Forman, *Phys. Rev. B*, 1975, **12**, 20.

44 P. Y. Yu and Y. R. Shen, *Phys. Rev. B*, 1975, **12**, 1377.

45 H. Y. Zhao, Y. F. Wang and J. H. Zeng, *Cryst. Growth Des.*, 2008, **8**, 3731–3734.

46 H. Yu, J. Yu, S. Liu and S. Mann, *Chem. Mater.*, 2007, **19**, 4327–4334.

47 Q. Hua, D. Shang, W. Zhang, K. Chen, S. Chang, Y. Ma, Z. Jiang, J. Yang and W. Huang, *Langmuir*, 2011, **27**, 665–671.

48 D. Cai, D. Wang, B. Liu, Y. Wang, Y. Liu, L. Wang, H. Li, H. Huang, Q. Li and T. Wang, *ACS Appl. Mater. Interfaces*, 2013, **5**, 12905–12910.

49 J. Liu, M. Chen, L. Zhang, J. Jiang, J. Yan, Y. Huang, J. Lin, H. J. Fan and Z. X. Shen, *Nano Lett.*, 2014, **14**, 7180–7187.

50 F. Zhang, C. Yuan, J. Zhu, J. Wang, X. Zhang and X. W. Lou, *Adv. Funct. Mater.*, 2013, **23**, 3909–3915.

51 Y. He, W. Chen, X. Li, Z. Zhang, J. Fu, C. Zhao and E. Xie, *ACS Nano*, 2013, **7**, 174–182.

52 G. Wang, J. Huang, S. Chen, Y. Gao and D. Cao, *J. Power Sources*, 2011, **196**, 5756–5760.

53 R. Kumar, K. Jahan, R. K. Nagarale and A. Sharma, *ACS Appl. Mater. Interfaces*, 2015, **7**, 593–601.

54 L. Gao, X. Wang, Z. Xie, W. Song, L. Wang, X. Wu, F. Qu, D. Chena and G. Shen, *J. Mater. Chem. A*, 2013, **1**, 7167–7173.

55 J. Yan, Q. Wang, T. Wei and Z. Fan, *Adv. Energy Mater.*, 2014, **4**, 1300816.

56 P. Rai, W.-K. Kwak and Y.-T. Yu, *ACS Appl. Mater. Interfaces*, 2013, **5**, 3026–3032.

57 J. Tamaki, J. Niimi, S. Ogura and S. Konishi, *Sens. Actuators, B*, 2006, **117**, 353–358.